Heliyon 9 (2023) e14488

Contents lists available at ScienceDirect

Heliyon

journal homepage: www.cell.com/heliyon

Research article

Phenol red dye removal from wastewater using TiO_2-FSM-16 and Ni-FSM-16 photocatalysts

Seyed Mohamadsadegh Mousavi [a], Seyed Hamed Meraji [a,**], Ali Mohammad Sanati [b,***], Bahman Ramavandi [c,*]

[a] Department of Civil Engineering, Persian Gulf University, Bushehr, Iran
[b] Department of Environmental Science, Persian Gulf Research Institute, Persian Gulf University, Bushehr, Iran
[c] Systems Environmental Health and Energy Research Center, The Persian Gulf Biomedical Sciences Research Institute, Bushehr University of Medical Sciences, Bushehr, Iran

ARTICLE INFO

Keywords:
Degradation
Leaching
Phenol red
Titanium dioxide
Photocatalyst

ABSTRACT

In this study, the performance of Ni-FSM-16 and TiO_2-FSM-16 photocatalysts in phenol red removal was explored. The XRD, FE-SEM, and BET tests were used to characterize the catalysts. All experiments were performed at ambient temperature and under UV (20 W). The parameters including dye concentration (20–80 mg/L), photocatalyst concentration (0–8 g/L), UV exposure duration, and contact time (0–160 min) were optimized using RSM software. BET values of Ni-FSM-16 and TiO_2-FSM-16 were 718.63 m^2/g and 844.93 m^2/g, respectively. TiO_2-FSM-16 showed better performance in dye removal than Ni-FSM-16. At pH 3, the maximum dye removal by TiO_2-FSM-16/UV and Ni-FSM-16/UV was obtained 87% and 64%, respectively. The positive hole species had the main role in photocatalytic phenol red removal. The reusability study was done for up to 7 cycles, but the catalysts can be reused effectively for up to 3 cycles. The synergistic factor for the TiO_2-FSM-16 and TiO_2-FSM-16/UV processes were calculated to be 1.55 and 2.12, respectively. The dye removal efficiency by TiO_2-carbon and Ni-carbon was slightly lower than those obtained by the FSM-16 ones. The TiO_2-FSM-16 and Ni-FSM-16 catalysts had a suitable surface and acceptable efficiency in phenol red removal.

1. Introduction

Dyes are mainly used in the plastics, textile, paper, rubber, wood, and food industries [1]. The presence of colorant materials in streams is not only aesthetically unpleasant but can also cause problems for the environment by elevating toxicity, oxygen demand levels, and lagging the photosynthetic phenomena by reducing light penetration [2,3]. Dyes belonging to the groups based on anthraquinone, azo, and triphenylmethane are the main pollutants released from industrial effluents [4,5]. Most of the dye laden-effluents are produced by the textile industry, where 10–15% of the dye is wasted during the production process [4,6]. One of the dyes released from the textile is phenol red. Its solubility in water and ethanol is 0.77 g/L and 2.9 g/L, respectively [7]. Phenol red dye is water-soluble and can be utilized as a pH indicator in various laboratories [8,9]. This dye is used in industries such as

* Corresponding author.
** Corresponding author.
*** Corresponding author.
E-mail addresses: h.meraji@pgu.ac.ir (S.H. Meraji), sanati@pgu.ac.ir (A.M. Sanati), b.ramavandi@bpums.ac.ir (B. Ramavandi).

https://doi.org/10.1016/j.heliyon.2023.e14488
Received 17 January 2023; Received in revised form 27 February 2023; Accepted 8 March 2023
Available online 11 March 2023

pharmaceuticals, textiles, and chemicals, and the wastewater discharged from these industries must be properly treated [9].

Various physical, chemical, and biological methods have been tested to eliminate dyes. Physical and chemical methods can be used on a small scale [10]. Advanced oxidation methods (AOMs) have been considered by researchers for cleaning effluents containing resistant organic compounds [11,12]. AOMs are based on the production of active species for degrading pollutants using solar, chemical, or other forms of energy [13,14]. The photocatalytic oxidation process is a superficial phenomenon and light reactions happen on the catalyst surface like TiO_2 [11,15]. Titanium dioxide (TiO_2) has so far been considered comparable to other semiconductors for many reasons, including its cheapness, availability, safety, and good reactivity [11,16]. Also, it can degrade organic compounds and as a result, the pollutants are converted to H_2O and CO_2 [16]. Nickel is also a useful photocatalyst that has low cost and good stability in alkaline solutions [17]. However, it is difficult to use titanium dioxide and nickel alone because their separating from the solution is a time-consuming and costly process. Therefore, the photocatalyst should be stabilized on a support surface. Many supporting surfaces like activated carbon [18], graphene oxide [19], silicate [20], and glass spheres [21] have been used for titanium dioxide and nickel oxide.

The FSM-16 powder has outstanding features like high thermal stability, high specific surface area, and high pollutant sorption capacity, which makes it a suitable option for photocatalyst support. Although FSM-16 has been used to support photocatalysts to decompose some pollutants [22,23], its application as support of titanium dioxide and nickel oxide in dye removal is not yet clear.

Accordingly, the main aim of this study was to evaluate the photocatalytic activity of TiO_2-FSM-16 and Ni-FSM-16 in phenol red degradation. Phenol red decomposition using TiO_2-FSM-16 and Ni-FSM-16 was examined in the presence of UV rays and the effect of operating parameters was studied. The characteristics of photocatalysts, reaction kinetics, catalyst reusability, leaching of the photocatalyst components, and synergy of process components have also been investigated. In another part of the work, the dye removal efficiency of TiO_2-FSM-16 and Ni-FSM-16 was compared with TiO_2-carbon and Ni-carbon.

2. Experimental

2.1. Materials

Acetyl trimethylammonium bromide ($C_{19}H_{42}BrN$, purity >99.9%), hydrochloric acid (HCl, 37 wt%), sodium hydroxide (NaOH, purity >99.9%), silicon dioxide (SiO_2, purity >99.8%), ammonium titanyl oxalate monohydrate ($(NH_4)_2TiO(C_2O_4)_2{\cdot}H_2O$, purity: 98%), ethanol (C_2H_6O, purity ≥99.9%), nickel nitrate ($Ni(NO_3)_2$, purity> 99.8%) were purchased from Merck Company. Phenol red ($C_{19}H_{14}O_5S$, purity: 98%), *tert*-butanol alcohol ($C_4H_{10}O$, purity ≥99.5%), *p*-benzoquinone ($C_6H_4(=O)$, purity >98%), silver nitrate ($AgNO_3$, purity ≥99%), and ammonium oxalate ($(NH_4)_2C_2O_4{\cdot}H_2O$, purity ≥99.99%) were provided from Sigma-Aldrich Company. The stock solution of the phenol red dye was prepared daily in doubly distilled water (DDW). All working solutions were prepared by diluting the stock with DDW.

2.2. Measurements

Morphology of FSM-16, TiO_2-FSM-16, and Ni-FSM-16 was done using the TeScan-Mira III Scanning Field Emission Microscope (FE-SEM, Czech Republic). Nitrogen absorption-desorption test was performed by BET instrument, Micrometric model ASAP2020 (USA). The XRD pattern was taken by the PANalytical manufacturer, Xpert-pro model (USA) at 2θ equal to 0.5–60° and CuKα of 1.5406 nm. Phenol red content was determined by UV–vis spectrophotometer, PerkinElmer, Lambda 25 (USA) at λ_{max} 423 nm. An example of a calibration curve to determine the concentration of phenol red is presented in Fig. S1 in the Supplementary Information. The amount of dye mineralization was measured by the TOC device (Shimadzu, model VCSH, Japan).

2.3. Synthesis of FSM-16

First, 3.8 g NaOH was added to 100 mL of DDW and 6 g of SiO_2 was poured into the solution to make the SiO_2/Na_2O ratio equal to 2. It was then stirred for 3 h under normal conditions at ambient temperature (27 °C) to obtain a uniform solution. To remove the available solvent, the sample was placed in a rotary evaporator balloon. The evaporator temperature was set to 100 °C and the speed was 30 rpm. Approximately 60–70 mL of water was evaporated and resulted in a jelly-like liquid of sodium silicate. Finally, the sample was poured into a porcelain plate and transferred to a furnace to complete the synthesis and calcination process of layered sodium silicate. The furnace was programmed with a temperature rate of 2 °C/min at 700 °C for 6 h. The calcined sample was layered sodium silicate or Kanemite. This material was crushed in a mortar and 4 g of it was poured into 40 mL of DDW and agitated for 3 h at 27 °C. After the preparation of Kanemite paste, which was used as a source of silica in the synthesis of regular mesopores of FSM-16. Through a mechanism, the Kanemite silicate plates were folded and cross-linked to form a three-dimensional structure. To make a wet Kanemite paste, the resulting solution was filtered. The Kanemite was dispersed in 88 mL of n-hexadecyl trimethyl ammonium bromide solution (0.125 mol/L) and stirred for 3 h at 70 °C. In this step, pH should be adjusted between 11.5 and 12.5. After that, the pH was decreased to 8.5 using 2 mol/L HCl. The suspension solution was stirred for 3 h at 70 °C. The produced material was then washed at room temperature with a liter of distilled water and air-dried. The synthesized meso-cavity was placed in the Soxule device for washing. Washing was done with 20 mL of ethanol and 0.5 mL of HCl per gram of material. The meso-cavity material was placed in a Soxule device for 72 h. The material was then dried for 24 h at ambient temperature. Finally, it was placed in the furnace (950 °C, 9 h) to remove the surfactant [24].

2.4. Synthesis of TiO_2-FSM-16 and Ni-FSM-16

To deposit titanium dioxide on FSM-16, a solution with a concentration of 0.1 M of titanium oxalate ammonium salt was prepared. Then, 2 g of FSM-16 was added to 25 mL of titanium solution. The sample was stirred at room temperature for 24 h. After filtering and washing the samples with DDW and air-drying, the samples were calcined at 450 °C for 12 h [25].

To make the Ni-FSM-16 catalyst, initially, 1 g of FSM-16 mesoporous silica was dissolved in 20 mL of normal hexane and stirred at room temperature for 2 h (Solution A). The amount of 0.5675 g of nickel nitrate was added to another vessel with 1.14 mL of DDW (Solution B). After 2 h, Solution B was added dropwise to Solution A and the new mixture was stirred for 3 h. It was then air-dried for 24 h. The solids were subjected to argon gas for calcination at 550 °C for 5 h. The gradient for increasing and decreasing the temperature at this stage was 2.5 °C/min and the flow rate of argon gas injection into the furnace was 2 L/h [26].

2.5. Synthesis of TiO_2-carbon and Ni-carbon

To make TiO_2-carbon and Ni-carbon, the same methods as TiO_2-FSM-16 and Ni-FSM-16 were done. It should be noted that activated carbon in this study was purchased from Merck and according to the supplier's information, it had an active surface of 810 m^2/g.

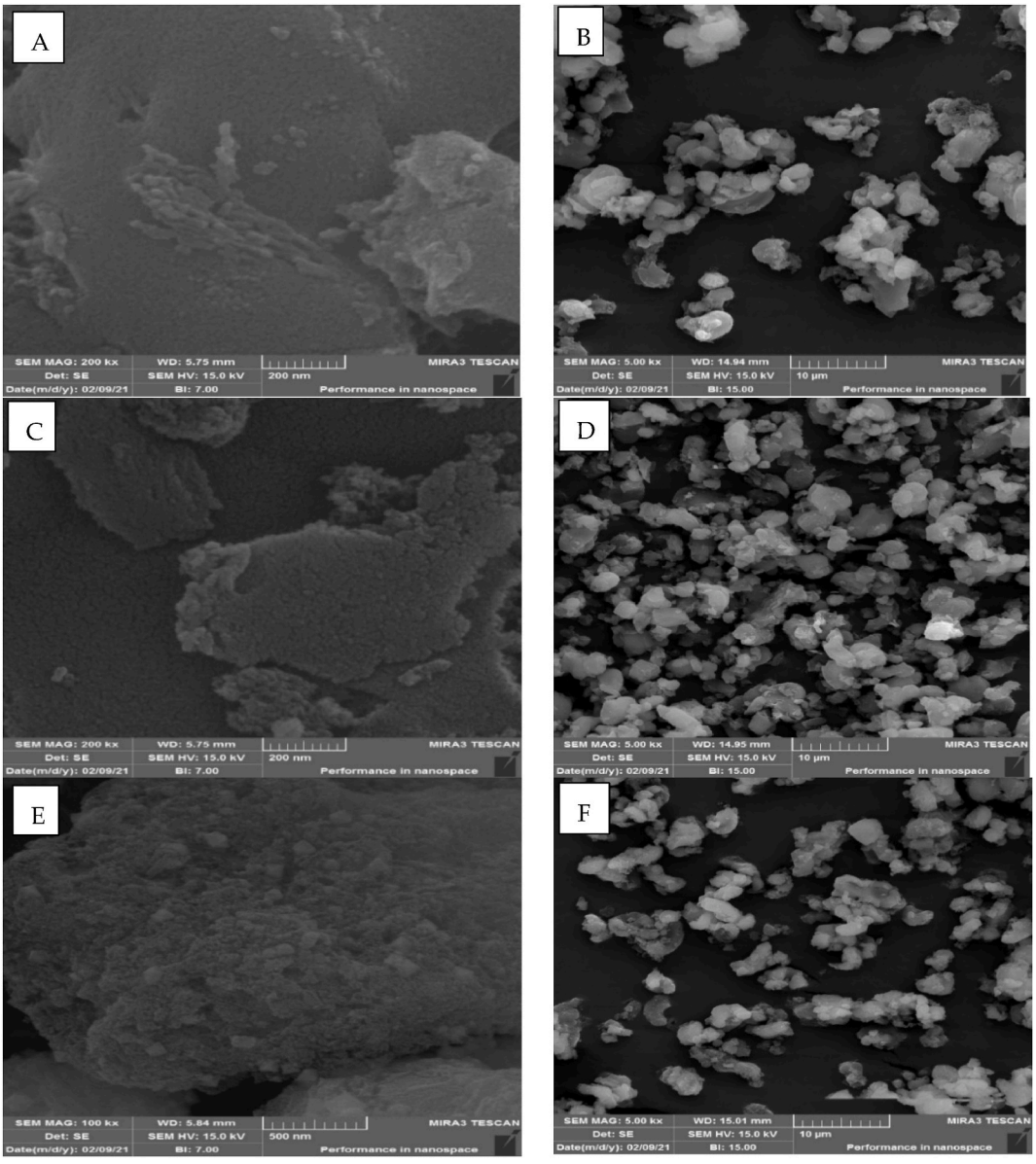

Fig. 1. FE-SEM images of FSM-16 **(A)** 200 nm **(B)** 10 µm, TiO_2-FSM-16 **(C)** 200 nm **(D)** 10 µm, and Ni- FSM -16 **(E)** 500 nm **(F)** 10 µm.

2.6. Design of experiments using a response surface methodology (RSM)

Four factors were analyzed by the response surface method. The effect of four experimental variables, namely TiO_2-FSM-16 and Ni-FSM-16 quantity, solution pH, UV irradiation time, and dye concentration on the photocatalytic removal of phenol red was explored. The variables and their upper and lower levels are listed in Table S1 in the Supplementary Information.

A total of 30 tests were performed, including 16 experiments at factorial points, 8 experiments at axial points, and 6 replications at central points.

The efficiency of dye removal was calculated using the following equation:

$$\text{Dye removal } (\%) = \frac{\left([\text{Dye}]_{\text{initial}} - [\text{Dye}]_{\text{residual}}\right)}{[\text{Dye}]_{\text{initial}}} \text{ x } 100 \quad (1)$$

2.7. Recovery test

The photocatalysts (TiO_2-FSM-16 and Ni-FSM-16) were recovered after being used in dye removal. The photocatalysts were separated using a centrifuge, washed (with water and ethanol), dehydrated (at 105 °C), and then reused for dye degradation. The reusability tests were done 7 times.

2.8. Effect of scavengers

Compounds of *tert*-butanol (500 mM), *p*-benzoquinone (10 mM), silver nitrate (10 mM), and ammonium oxalate (50 mM) were used as scavengers of active species and radicals in the process of phenol red removal [27]. This test was performed at optimal conditions (pH: 3, dye concentration: 20 mg/L, catalyst dose: 2 g/L, time: 120 min).

3. Results and discussion

3.1. Main properties of photocatalysts

The micrographs (FESEM) of the FSM-16 are presented in Fig. 1A, B. Based on the FESEM graphs, nanoparticles with an approximate size of 200 nm were observed. In the study conducted by Hashemi et al., the FSM-16 nanoparticles have a spherical shape with a size of 100 nm [28]. The FESEM images of TiO_2-FSM-16 are shown in Fig. 1C,D. As this figure shows, the photocatalyst particles are non-uniform and spherical. TiO_2-FSM-16 particles have a similar shape to those reported in other works [22]. This particle size distribution with spherical morphology corresponded to van der Waals forces [29]. To decrease the surface energy, the primary particles tend to condense, with the formation of spherical masses, in the minimum surface-to-volume ratio, the minimum free surface energy can be obtained. The TiO_2-FSM-16 composite powder is composed of nanoscale particles, which indicates that the prepared powder has a large specific surface area and volume. Therefore, the TiO_2-FSM-16 composite can provide suitable active sites for photocatalysis. Fig. 1C,D shows that TiO_2 particles are dispersed on the surface of SiO_2 nanoparticles and have good stability.

The shape and size of crystals in Ni-FSM-16 are slightly different from TiO_2-FSM-16 (Fig. 1E,F). The Ni-FSM-16 particles have a small size and are aggregates of spherical microcrystal particles. Silicate plates are a combination of tens to hundreds of hexagonal cavities composed of Ni-FSM-16 catalyst particles. Adhesion between particles may be due to the small magnetism or the polymer between them [30,31].

The XRD image of FSM-16, TiO_2-FSM-16, and Ni-FSM-16 is shown in Fig. 2. A wideband with an angle equal to 20–30° can be seen in the FSM-16 spectrum, revealing that the material is amorphous and has no specific crystalline peaks. The disappearance of the higher-order diffraction peaks indicates that the hexagonal arrangement of the channels in the TiO_2-FSM-16 and Ni-FSM-16 mesoporous materials is slightly irregular. Therefore, it can be concluded that the addition of metal in the mesoporous structure of FSM-16 has a negative effect on the crystallinity of the material. This is because the use of metal ores weakens the self-assembly process and produces a less regular meso-cavity structure. In the XRD pattern of TiO_2-FSM-16 and Ni-FSM-16, in addition to the four distinct peaks of the FSM-16 nanoparticles, the characteristic peaks of TiO_2 and NiO are also seen, indicating no noticeable change in the crystal

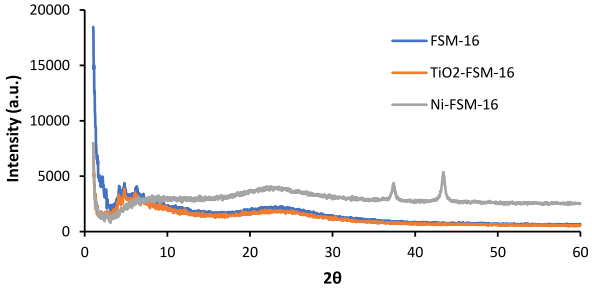

Fig. 2. X-ray diffraction pattern of FSM-16, TiO_2-FSM-16, and Ni-FSM-16.

structure of the photocatalysts [32]. The low-angle XRD image of FSM-16 showed that the diffraction plate has a regular hexagonal structure [33]. An anatase-like reference pattern (JCPDS # 21–1272) was seen in TiO_2-FSM-16 [34]. Five peaks at 37, 43, 48, 52, and 58 in Ni-FSM-16 photocatalyst are related to Miller indices of (111), (200), (220), (311), and (222), respectively, which confirms that the photocatalyst contains NiO [35–37]. Based on the literature [38], a main reflection at 2theta of 43.5°, corresponds to the (200) plane of cubic NiO (PDF-2, 01–071–1179).

The active area of the photocatalysts was computed using Brunauer-Emmett-Teller (BET) technique and the pore diameter and pore volume were calculated by the BJH technique (Fig. 3a–c). For the FSM-16 sample, the obtained BET was 1099.08 m^2/g, and the absorption isotherm is almost synchronous with the desorption branch, indicating the mesoporous structure of the sample. Fig. 3b and c shows a similar pattern of BET for TiO_2-FSM-16 (844.93 m^2/g) and Ni-FSM-16 (718.63 m^2/g), showing that the mesoporous feature of FSM-16 did not alter after the composition with Ni and TiO_2 [39].

The specific surface area of Ni-FSM-16 and TiO_2-FSM-16 was lower than that of FSM-16, which is linked to the occupation of pores by Ni and TiO_2 (Fig. 3). However, the level of synthesized photocatalyst (844.93 m^2/g) is much bigger than the values stated for other photocatalysts in the literature. For example, Fatima and Supia prepared the TiO_2-MCM-41 photocatalyst with a surface of 400.7 m^2/g [40]. Sugiyama et al. have incorporated Ni into FSM-16 and MCM-41 structures to produce Ni-FSM-16 and Ni-MCM-41 and reported that the active surface of photocatalysts was lower than that of the base material [41].

3.2. Interpretation of ANOVA and interaction of variables

ANOVA was utilized to determine the relationship between the removal rate and the variables. It is noteworthy that the judgment was based on the F-values and P-values for phenol red removal. The F-values of the model for TiO_2-FSM-16 and Ni-FSM-16 were obtained at 16.77 and 12.16, respectively, indicating that the models are significant. The P-value was <0.05 indicating the significance

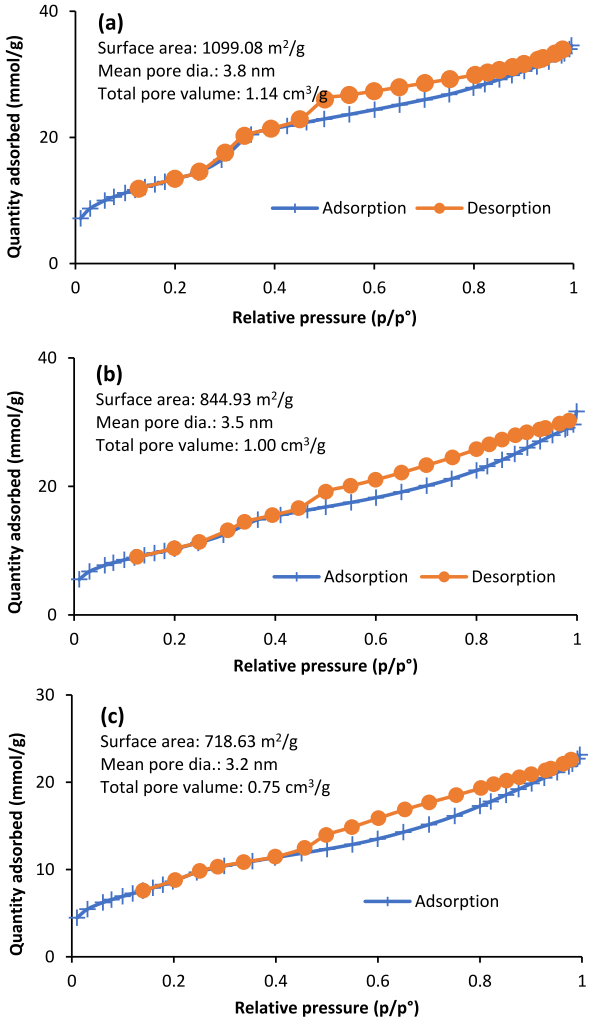

Fig. 3. BET graphs for **(a)** FSM-16, **(b)** TiO_2-FSM-16, and **(c)** Ni-FSM-16.

of the model expression. In this case, the 'A' variable in TiO_2-FSM-16 and 'A, B, and D' in Ni-FSM-16 were significant. In addition, the validity of the design with values of P and high value of correlation coefficients as well as the non-significance of "Lack of Fit" is confirmed [42]. $P < 0.0001$ reveals the importance of the model and the interaction of variables on phenol red elimination. The pH factor played an important role in phenol red removal using both photocatalysts (TiO_2-FSM-16 and Ni-FSM-16) with the biggest F-value (60.56 and 133.57, respectively) compared to other variables (Table S2 and S3). To evaluate the quality of the models, the figures for the predicted response *vs* the actual values and the normal data distribution diagrams are shown in Fig. S2. The normal diagram of the residues is provided in Fig. S2a,c. Such a graph is very useful for optimizing complex systems such as multivariate optimization. The points are in a straight line and no deviations are seen in the distribution of data, indicating a suitable correlation and distribution between the values [43]. Since the specific trend is not related to variance changes (decrease or increase), the variance is fixed, which shows the scatter of points against the given values (Fig. S2b,d).

Investigation of the effect of the desired catalysts (TiO_2-FSM-16 and Ni-FSM-16) on phenol red degradation efficiency under ultraviolet radiation is depicted in Fig. S3a. In this figure, the positive and negative effects and the magnitude of the effect of each variable on the response are identified. The sharpness of the slope in a factor indicates that it is a vital variable in the reaction [5]. Oppositely, a relatively flat line shows the insensitivity of the response to alteration in the given variable. As can be seen in Fig. S3a, the TiO_2-FSM-16 curve shows the time and dye concentration of the slow curvature, showing that these factors have a small effect on the response. Accordingly, the significant sloping curvature at pH indicates that the phenol red removal was sensitive to this variable. Fig. S3b shows that the curvature time and dye concentration have a slow slope, indicating that the mentioned factors have a small impact on the response.

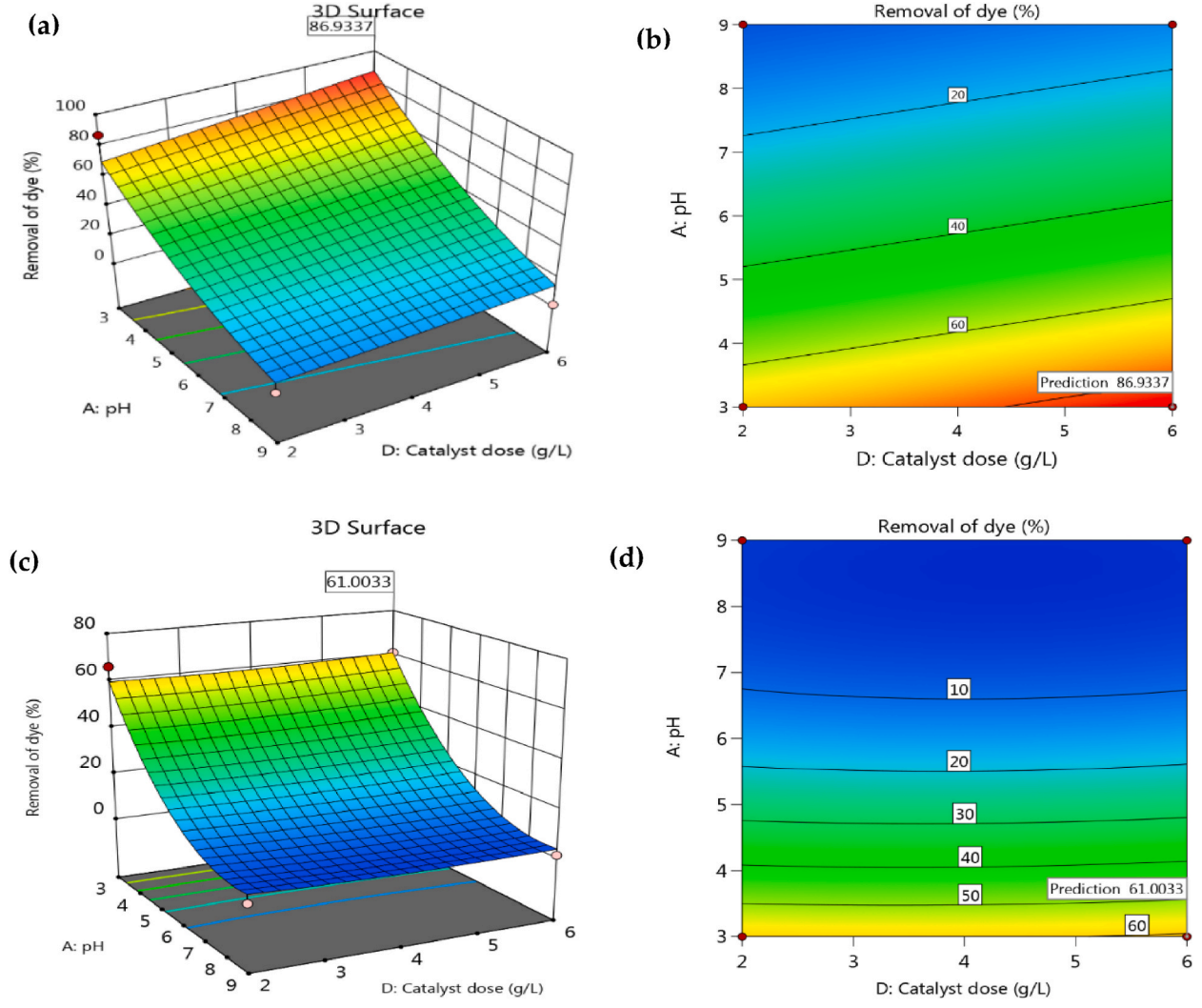

Fig. 4. 3D and 2D diagrams of the interactions of pH-photocatalyst dose on the phenol red removal in the presence of **(a,b)** TiO_2- FSM-16 and **(c,d)** Ni-FSM-16.

3.3. Effect of pH-photocatalyst dose

In Fig. 4a–d, the response surface (3D surfaces) and contour diagrams (2D contours) are depicted as a function of pH and photocatalyst dose. For both generated materials (TiO_2-FSM-16 and Ni-FSM-16), while the irradiation time (120 min) and the phenol red concentration (20 mg/L) were constant, the amount of degradation decreases with increasing pH. In other words, for both catalysts, the highest efficiency occurred at pH 3. At acidic pHs, the phenol red molecule has the zwitterion form with two functional groups (sulfate with a negative charge and ketone with a positive charge) with an additional proton. The FSM-16-TiO_2 surface also has protonated functional groups at low pH. The dye molecule has positive and negative charges at low pH. Therefore, the maximum efficiency at the acidic pH of 3 is due to the electrostatic attraction between protonated groups and zwitterion negative charges [44]. If the pH of the solution is higher than the pKa of phenol red (about 7.9), the proton of the ketone group is lost and the molecule takes on a negative charge [45]. The higher the pH, the more negative the catalyst level becomes (pHzpc of both photocatalysts was about 5.4). In such a situation, the dye molecule is rejected from the surface of the catalysts, and as a result, the removal efficiency decreases. Kumar et al. [46] reported that at acidic pHs, the surface of titanium dioxide becomes positive, leading to higher dye removal.

With the increasing load of TiO_2-FSM-16, a slight change in removal efficiency was observed. This has been linked to the tendency of particles to accumulate, which reduces the BET area of the catalyst and leads to less production of active radicals [47,48]. For the Ni-FSM-16, increasing the photocatalyst mass did not play a role in increasing the efficiency and the graph was smooth. Higher content

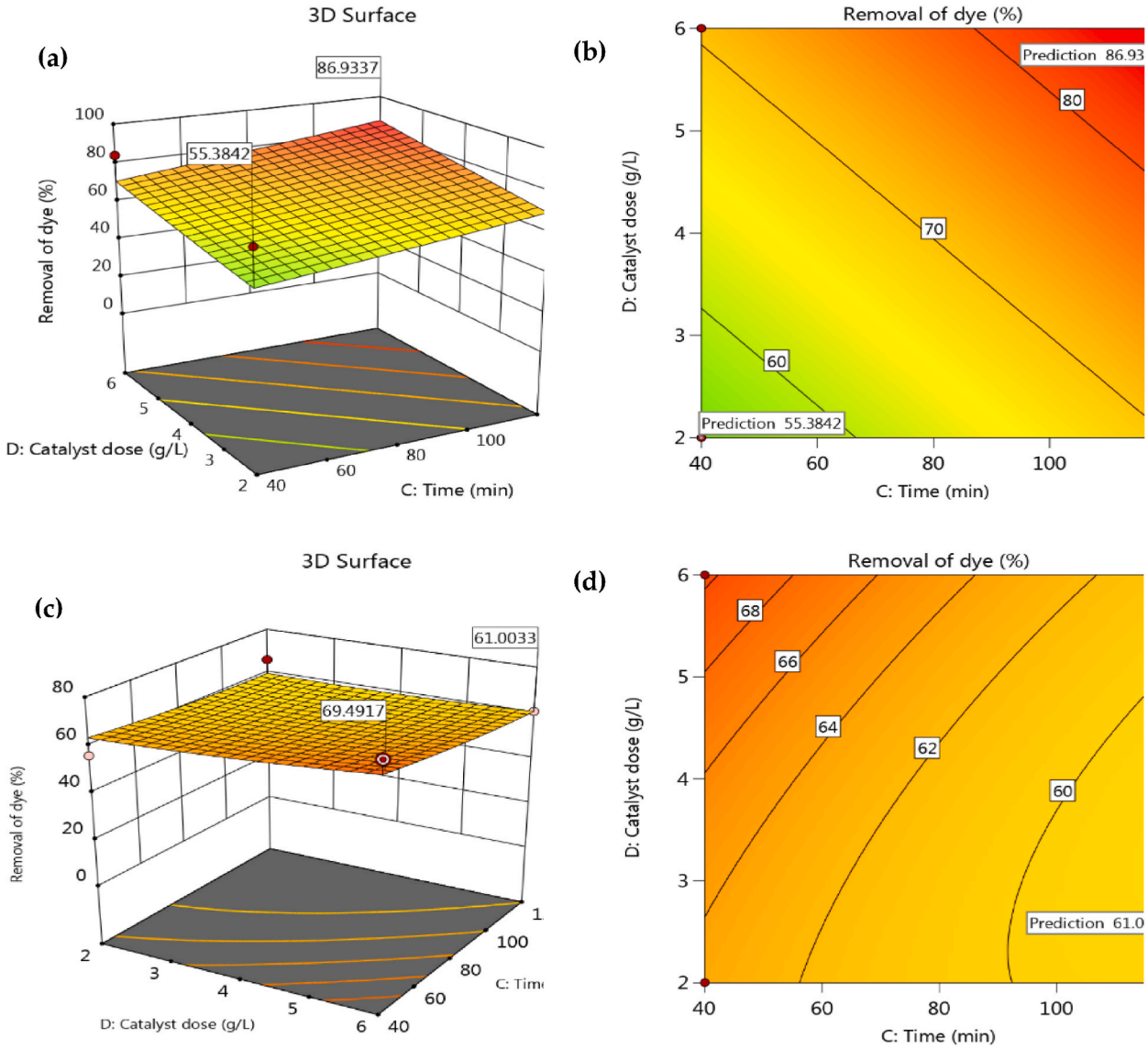

Fig. 5. 3D and 2D diagrams of the interactions of time-photocatalyst dose on the phenol red removal in the presence of **(a,b)** TiO_2- FSM-16 and **(c, d)** Ni-FSM-16.

of TiO_2-FSM-16 than Ni-FSM-16 can lead to more radical production and thus higher efficiency [25]. Similar observations have been reported by researchers for degrading cephalexin using NiS and NiS-support Fe_3O_4@PPY photocatalysts [49].

3.4. Effect of time-photocatalysts dose

The effect of treatment time and photocatalyst dose on the phenol red elimination is depicted in Fig. 5a–d. As shown in Fig. 5, increasing the dose of TiO_2-FSM-16 photocatalyst has resulted in a slow increase in the removal efficiency, while with increasing Ni-FSM-16 the efficiency has remained almost constant. With more time of exposure of TiO_2 nanoparticles to light, the dye removal efficiency increases. Longer exposure to light implies the production of more hydroxyl radicals, which are responsible for the oxidation of the phenol red dye molecule [50].

With increasing filtration time, the amount of dye removal by the TiO_2-FSM-16 photocatalyst increased due to the sufficient opportunity for radicals to attack the dye. But with increasing time, the removal efficiency by Ni-FSM-16 decreases, which is probably due to the desorption of absorbed dye from the catalyst surface. So, it can be confirmed that the Ni-FSM-16 photocatalyst may not have been able to oxidize the dye but rather remove it by the adsorption process.

3.5. Photocatalyst reusability and leaching Ni and ti

A recyclable photocatalyst would be economically and environmentally beneficial. The photocatalyst recovery results are shown in Fig. 6a. Based on Fig. 6a, the reusability behavior of the two produced materials was different. The TiO_2-FSM-16 photocatalyst has higher usability and good strength. TiO_2-FSM-16 catalyst could be reused up to 3 times, while Ni-FSM-16 had up to 2 times good removal efficiency. The reduction in the efficiency of the recycled catalyst can be due to the leakage of its effective components. In these two photocatalysts, nickel and titanium are important components. The results of Fig. 6b show that these elements have leaked from the photocatalyst. Another significant point is that the amount of nickel leakage is lower than the drinking water standard (100 μg/L). Among the two prepared catalysts, the amount of leakage in TiO_2-FSM-16 was lower, which indicates its stability and, as a result, its higher efficiency.

3.6. Synergy of system components in the removal of phenol red

In Fig. 7, the effect of system components on the removal efficiency of phenol red dye is compared with the whole system. As depicted in this figure, the efficiency of the system components and even UV along with nickel and titanium dioxides were much lower than the whole system. FSM-16 has been reported to have a 51% removal of phenol red, possibly due to the adsorption mechanism. The high surface of the FSM-16 material has also provided a suitable platform for dye adsorption. The synergy factor for the TiO_2-FSM-16/UV was calculated based on the following formulas [51]:

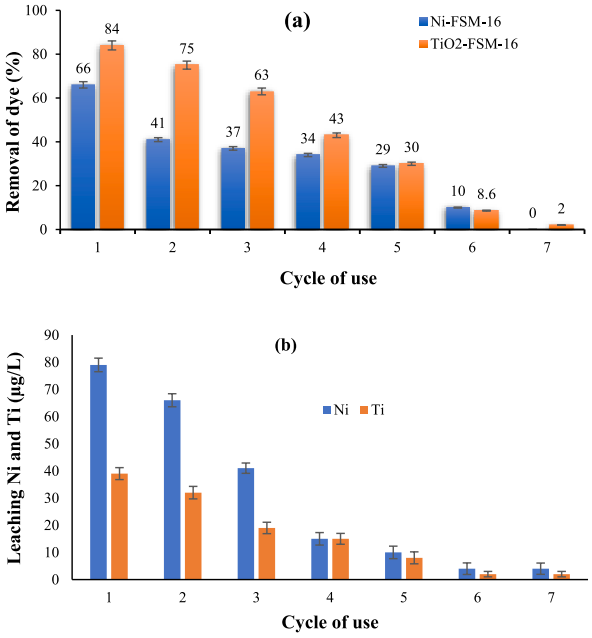

Fig. 6. (a) Photocatalysts reusability (pH: 3, dye concentration: 20 mg/L, catalyst dose: 2 g/L, time: 120 min) and **(b)** leaching Ni and Ti from the photocatalysts (pH: 3, dye concentration: 20 mg/L, catalyst dose: 2 g/L, time: 120 min).

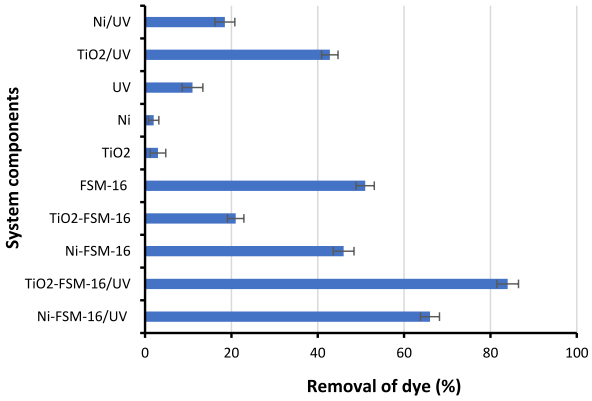

Fig. 7. Effect of the system components on phenol red removal (pH: 3, dye concentration: 20 mg/L, catalyst/adsorbent dose (if applicable): 2 g/L, time: 120 min).

$$\text{Synergy factor}_{\text{TiO2-FSM-16}} = \frac{k_{obs}^{\text{TiO2-FSM-16}}}{k_{obs}^{\text{TiO2}} + k_{obs}^{\text{FSM-16}}} \tag{2}$$

$$\text{Synergy factor}_{\text{TiO2-FSM-16/UV}} = \frac{k_{obs}^{\text{TiO2-FSM-16/UV}}}{k_{obs}^{\text{TiO2}} + k_{obs}^{\text{FSM-16}} + k_{obs}^{\text{UV}}} \tag{3}$$

The synergistic factor for the TiO_2-FSM-16 and TiO_2-FSM-16/UV processes were computed at 1.55 and 2.12, respectively. These findings reveal the effective interaction of UV, TiO_2, and FSM-16 components with each other that lead to elevated degradation of phenol red dye.

3.7. Effect of scavengers

Components like hydroxyl radicals (OH•), superoxide (O_2^-•), photogenerated holes ($h\vartheta^+$), and electrons (e^-) can be effective in the photocatalytic dye removal process [52–54]. According to scientific papers [43,47], the compounds of *tert*-butanol, *p*-benzoquinone, silver nitrate, and ammonium oxalate are effective in abducting the active components of hydroxyl radicals (OH•), superoxide (O_2^-•), electrons, and photogenerated holes ($h\vartheta^+$), respectively. To clarify the decomposition mechanism, the effect of these scavengers on dye removal efficiency was explored and the results are drawn in Fig. 8a. According to Fig. 8a, it is clear that the amount of dye removal has decreased with the addition of scavengers. The most severe decrease in phenol red removal efficiency was for ammonium oxalate,

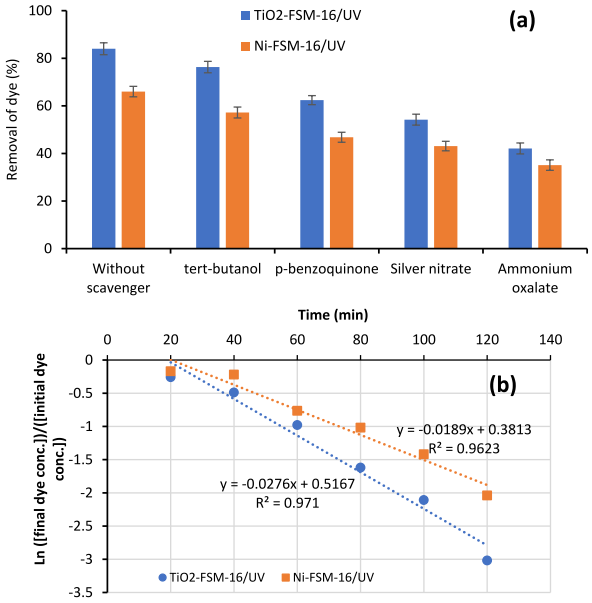

Fig. 8. **(a)** Effect of scavengers on phenol red removal by the developed system (pH: 3, dye concentration: 20 mg/L, catalyst dose: 2 g/L, time: 120 min) and **(b)** kinetic of the dye degradation process (pH: 3, dye concentration: 20 mg/L, catalyst dose: 2 g/L).

followed by silver nitrate, *p*-benzoquinone, and *tert*-butanol. This indicates that photogenerated holes ($h\vartheta^+$) were the most effective species in the photocatalytic process of phenol red removal. Similar results have been stated for the catalytic elimination of *p*-aminophenol and methylene blue dye by TiO_2/RGO catalyst [47] and Brilliant green by $MgFe_2O_4$ catalyst [43].

3.8. Kinetic of the dye degradation process

The kinetics of the phenol red degradation process was evaluated under optimal conditions (see Fig. 8b). The first-order equation was utilized to assess the kinetic behavior of phenol red catalytic decontamination:

$$\mathrm{Ln}\frac{[\text{final dye conc.}]}{[\text{initial dye conc.}]} = -\mathrm{k.t} \quad (4)$$

If the graph $\mathrm{Ln}\frac{[\text{final dye conc.}]}{[\text{initial dye conc.}]}$ *vs* time is drawn, a line is attained, and its slope is the reaction rate constant (k, min^{-1}). As shown in Fig. 8b, the data follow first-order kinetics ($R^2 > 0.96$). The phenol red photodegradation rate constant using TiO_2-FSM-16 and Ni-FSM-16 was calculated at 0.028 and 0.018 min^{-1}, respectively. The reaction rate with TiO_2-FSM-16 photocatalyst was about 1.5 times Ni-FSM-16. The kinetics of dye removal by various photocatalysts have followed the first-order model [43,52,55].

3.9. Mineralization test

The amount of dye mineralization was investigated by two photocatalysts. The results showed that under optimal conditions (pH: 3, dye concentration: 20 mg/L, photocatalyst dose: 2 g/L, time: 120 min), the amount of dye mineralization by TiO_2-FSM-16 and Ni-FSM-16 is 46% and 35%, respectively. It shows the effectiveness of the TiO_2-FSM-16 photocatalyst in dye removal compared to Ni-FSM-16. The results of this study are in the range of values reported for acid orange removal using $BiVO_4/TiO_2$ in the presence of H_2O_2 and $FeSO_4$ [56].

3.10. Literature comparison and comparison with TiO_2-carbon and Ni-carbon

Several methods have been reported so far for removing dyes. Among these methods, researchers emphasize the oxidation and adsorption of dyes. Table 1 compares the methods mentioned in scientific texts for dye removal with our method. As can be seen, concerning the conditions of the tests, the photocatalysts in this paper are among the satisfactory catalysts for dye removal.

As it is clear in Table 1, the laboratory conditions of previously published work are different from our work, and an exact comparison cannot be made. Therefore, activated carbon as the most famous base for the catalyst was made under the same conditions as the catalysts of TiO_2-FSM-16 and Ni-FSM-16 of this research and was investigated in the removal of the target pollutant. As shown in this table, the removal efficiency of carbon-based photocatalysts (BET: 810 m^2/g) is lower than that of FSM-based ones. These differences are probably due to the lower surface area that carbon provided for the reaction compared to FSM.

Table 1
Comparison of the methods mentioned in the literature for dye removal with the method used in this work.

Catalyst	Dye conc. (mg/L)	Dye	Catalyst mass (g/L)	UV irradiation time (min)	Removal (%)	Ref.
TiO_2nanosuspensions	3.2	Methylene blue	0.5	120	90	[57]
ZnO nanosuspensions	11	Methylene blue	1	60	100	[57]
Er/Pr-Codoped TiO_2/Poly (vinylidene difluoride)–Trifluoroethylene	10	Methylene blue	0.1	360	95	[58]
ZnO-Graphene	–	Methyl orange	–	360	89	[59]
$BaTiO_3$/graphene oxide	5	Methylene blue	0.5	180	95	[60]
Nb(5)/TiO_2 nanocomposite	20	Phenol red	0.1	160	94	[61]
TiO_2	20	Phenol red	0.1	160	79	[61]
(α-FeOOH) Goethite composite[a]	1770	Phenol red	1	90	96	[62]
TiO_2+H_2O_2+O_2 gas + irradiation	10	Phenol red	0.5	300	94	[63]
TiO_2-carbon	20	Phenol red	2	120	77	This work
Ni-carbon	20	Phenol red	2	120	64	This work
TiO_2-FSM-16	20	Phenol red	2	120	84	This work
Ni-FSM-16	20	Phenol red	2	120	66	This work

[a] This system has used irridation and H_2O_2 beside the catalyst.

4. Conclusions

In this study, TiO_2-FSM-16 and Ni-FSM-16 photocatalysts were produced and used to remove phenol red dye in the presence of UV light. The TiO_2-FSM-16 and Ni-FSM-16 photocatalyst had a BET area of 844.93 m^2/g and 718.63 m^2/g, respectively. Maximum phenol red removal using TiO_2-FSM-16 and Ni-FSM-16 was obtained at 84% and 66%, respectively under the conditions of pH 3, dye concentration of 20 mg/L, catalyst dose of 2 g/L, and irradiation time of 120 min. The photocatalyst activity of FSM-16 was increased after the corporation with TiO_2 and Ni. The synergistic factor of TiO_2-FSM-16 and TiO_2-FSM-16/UV processes were found to be 1.55 and 2.12, respectively. The TiO_2-FSM-16 photocatalyst with phenol red dye removal of 87% (TOC removal: 46%) had better activity than Ni-FSM-16 with 76% removal (TOC removal: 35%). Both photocatalysts, especially TiO_2-FSM-16, had good capabilities in removing phenol red dye.

Author contribution statement

Seyed Mohamadsadegh Mousavi: Conceived and designed the experiments; Performed the experiments.
Seyed Hamed Meraji: Analyzed and interpreted the data; Wrote the paper.
Ali Mohammad Sanati: Contributed reagents, materials, analysis tools or data; Performed the experiments.
Bahman Ramavandi: Analyzed and interpreted the data; Wrote the paper.

Funding statement

This research did not receive any specific grant from funding agencies in the public, commercial, or not-for-profit sectors.

Data availability statement

Data will be made available on request.

Additional information

Supplementary content related to this article has been published online at [URL].

Declaration of interest's statement

The authors declare no conflict of interest.

Acknowledgements

We are grateful to Bushehr University of Medical Sciences for access to laboratory equipment.

Appendix A. Supplementary data

Supplementary data related to this article can be found at https://doi.org/10.1016/j.heliyon.2023.e14488.

References

[1] M.A. Zazouli, A. Azari, S. Dehghan, R. Salmani Malekkolae, Adsorption of methylene blue from aqueous solution onto activated carbons developed from eucalyptus bark and Crataegus oxyacantha core, Water Sci. Technol. 74 (9) (2016) 2021–2035, https://doi.org/10.2166/wst.2016.287.
[2] M.M. Felista, W.C. Wanyonyi, G. Ongera, Adsorption of anionic dye (Reactive black 5) using macadamia seed Husks: kinetics and equilibrium studies, Sci. Afr. 7 (2020), e00283.
[3] C.H. Nguyen, M.L. Tran, T.T.V. Tran, R.-S. Juang, Enhanced removal of various dyes from aqueous solutions by UV and simulated solar photocatalysis over TiO_2/ZnO/rGO composites, Sep. Purif. Technol. 232 (2020), 115962.
[4] Y.-Q. Liu, N. Maulidiany, P. Zeng, S. Heo, Decolourization of azo, anthraquinone and triphenylmethane dyes using aerobic granules: acclimatization and long-term stability, Chemosphere 263 (2021), 128312.
[5] A. Azari, R. Nabizadeh, A.H. Mahvi, S. Nasseri, Magnetic multi-walled carbon nanotubes-loaded alginate for treatment of industrial dye manufacturing effluent: adsorption modelling and process optimisation by central composite face-central design, Int. J. Environ. Anal. Chem. (2021) 1–21.
[6] R. Jayalakshmi, J. Jeyanthi, Dynamic modelling of Alginate - cobalt ferrite nanocomposite for removal of binary dyes from textile effluent, J. Environ. Chem. Eng. 9 (1) (2021), 104924.
[7] M.R. Cyran, W.M. Dynkowska, A. Ceglińska, R. Bonikowski, Improving rye bread antioxidant capacity by bread-making methodology: contribution of phosphate-buffered saline- and methanol-soluble phenolic phytochemicals with different molecular profiles, J. Cereal. Sci. 100 (2021), 103262.
[8] P. Sri Sruthi, S. Balasubramanian, P. Senthil Kumar, A. Kapoor, M. Ponnuchamy, M. Mariam Jacob, S. Prabhakar, Eco-friendly pH detecting paper-based analytical device: towards process intensification, Anal. Chim. Acta 1182 (2021), 338953.
[9] A. Gautam, S. Rawat, L. Verma, J. Singh, S. Sikarwar, B.C. Yadav, A.S. Kalamdhad, Green synthesis of iron nanoparticle from extract of waste tea: an application for phenol red removal from aqueous solution, Environ. Nanotechnol. Monit. Manag. 10 (2018) 377–387.

[10] R.B. de Assis Filho, A.M.S. Baptisttella, C.M.B. de Araujo, T.J.M. Fraga, T.M.N. de Paiva, C.A.M. de Abreu, M.A. da Motta Sobrinho, Removal of textile dyes by benefited marine shells wastes: from circular economy to multi-phenomenological modeling, J. Environ. Manag. 296 (2021), 113222.

[11] V. Javanbakht, M. Mohammadian, Photo-assisted advanced oxidation processes for efficient removal of anionic and cationic dyes using Bentonite/TiO_2 nano-photocatalyst immobilized with silver nanoparticles, J. Mol. Struct. 1239 (2021), 130496.

[12] Q. Guan, G. Zeng, J. Song, C. Liu, Z. Wang, S. Wu, Ultrasonic power combined with seed materials for recovery of phosphorus from swine wastewater via struvite crystallization process, J. Environ. Manag. 293 (2021), 112961.

[13] Y. Liang, J. Li, Y. Xue, T. Tan, Z. Jiang, Y. He, W. Shangguan, J. Yang, Y. Pan, Benzene decomposition by non-thermal plasma: a detailed mechanism study by synchrotron radiation photoionization mass spectrometry and theoretical calculations, J. Hazard Mater. 420 (2021), 126584.

[14] Y. Wang, T. Sun, L. Tong, Y. Gao, H. Zhang, Y. Zhang, Z. Wang, S. Zhu, Non-free Fe dominated PMS activation for enhancing electro-Fenton efficiency in neutral wastewater, J.f Electroanal. Chem. 928 (2023), 117062.

[15] P. Xu, C. Ding, Z. Li, R. Yu, H. Cui, S. Gao, Photocatalytic degradation of air pollutant by modified nano titanium oxide (TiO_2) in a fluidized bed photoreactor: optimizing and kinetic modeling, Chemosphere (2023), 137995.

[16] K. Badvi, V. Javanbakht, Enhanced photocatalytic degradation of dye contaminants with TiO_2 immobilized on ZSM-5 zeolite modified with nickel nanoparticles, J. Clean. Prod. 280 (2021), 124518.

[17] K. Indira, S. Shanmugam, A. Hari, S. Vasantharaj, S. Sathiyavimal, K. Brindhadevi, A. El Askary, A. Elfasakhany, A. Pugazhendhi, Photocatalytic degradation of Congo red dye using nickel–titanium dioxide nanoflakes synthesized by *Mukia madrasapatna* leaf extract, Environ. Res. 202 (2021), 111647.

[18] A. Murugesan, M. Loganathan, P. Senthil Kumar, D.-V.N. Vo, Cobalt and nickel oxides supported activated carbon as an effective photocatalysts for the degradation Methylene Blue dye from aquatic environment, Sustain. Chem. Pharm. 21 (2021), 100406.

[19] T.-T. Pham, C. Nguyen-Huy, E.W. Shin, Facile one-pot synthesis of nickel-incorporated titanium dioxide/graphene oxide composites: enhancement of photodegradation under visible-irradiation, Appl. Surf. Sci. 377 (2016) 301–310.

[20] E. Binaeian, N. Seghatoleslami, M.J. Chaichi, H.-a. Tayebi, Preparation of titanium dioxide nanoparticles supported on hexagonal mesoporous silicate (HMS) modified by oak gall tannin and its photocatalytic performance in degradation of azo dye, Adv. Powder Technol. 27 (4) (2016) 1047–1055.

[21] V. Vaiano, O. Sacco, D. Sannino, P. Ciambelli, Nanostructured N-doped TiO_2 coated on glass spheres for the photocatalytic removal of organic dyes under UV or visible light irradiation, Appl. Catal., B 170–171 (2015) 153–161.

[22] A. Hosseini, H. Faghihian, Application of FSM-16 impregnated by TiO_2 as an efficient photocatalyst for elimination of benzothiophene and dibenzothiophene, adsorptive removal of degradation products by MCM-41, J. Ind. Eng. Chem. 76 (2019) 122–132.

[23] D. Jiraroj, O. Jirarattanapochai, W. Anutrasakda, J.S.M. Samec, D.N. Tungasmita, Selective decarboxylation of biobased fatty acids using a Ni-FSM-16 catalyst, Appl. Catal., B 291 (2021), 120050.

[24] B. Ohtani, Preparing articles on photocatalysis—beyond the illusions, misconceptions, and speculation, Chem. Lett. 37 (3) (2008) 216–229.

[25] H. Zabihi-Mobarakeh, A. Nezamzadeh-Ejhieh, Application of supported TiO2 onto Iranian clinoptilolite nanoparticles in the photodegradation of mixture of aniline and 2, 4-dinitroaniline aqueous solution, J. Ind. Eng. Chem. 26 (2015) 315–321.

[26] M. Tao, Z. Xin, X. Meng, Y. Lv, Z. Bian, Impact of double-solvent impregnation on the Ni dispersion of Ni/SBA-15 catalysts and catalytic performance for the syngas methanation reaction, RSC Adv. 6 (42) (2016) 35875–35883.

[27] Y. Shen, M.J. Martín de Vidales, J.C. Espíndola, A. Gómez-Herrero, A.J. Dos santos-García, Paracetamol degradation by photo-assisted activation of peroxymonosulfate over ZnxNi1−xFe_2O_4@BiOBr heterojunctions, J. Environ. Chem. Eng. 9 (6) (2021), 106797.

[28] S. Hashemi-Uderji, M. Abdollahi-Alibeik, R. Ranjbar-Karimi, FSM-16-SO3H nanoparticles as a novel heterogeneous catalyst: preparation, characterization, and catalytic application in the synthesis of polyhydroquinolines, Main Group Met. Chem. 41 (3–4) (2018) 91–101.

[29] N. Zhang, Y. Guo, Y. Guo, Q. Dai, L. Wang, S. Dai, W. Zhan, Synchronously constructing the optimal redox-acidity of sulfate and RuOx Co-modified CeO_2 for catalytic combustion of chlorinated VOCs, Chem. Eng. J. 454 (2023), 140391.

[30] G.-J. Lee, J.-H. Lee, D. Lee, K.-I. Park, C.K. Jeong, J.-J. Park, M.-K. Lee, Synthesis and characterization of carbon-coated Cu-Ni alloy nanoparticles and their application in conductive films, Appl. Surf. Sci. 566 (2021), 150672.

[31] Z. Huang, J. Ding, X. Yang, H. Liu, P. Song, Y. Guo, Y. Guo, L. Wang, W. Zhan, Highly efficient oxidation of propane at low temperature over a Pt-based catalyst by optimization support, Environ. Sci. Technol. 56 (23) (2022) 17278–17287.

[32] Z. Wu, C. Li, F. Zhang, S. Huang, F. Wang, X. Wang, H. Jiao, High-performance ultra-narrow-band green-emitting phosphor LaMgAl 11 O 19: Mn^{2+} for wide color-gamut WLED backlight displays, J. Mater. Chem. C 10 (19) (2022) 7443–7448.

[33] W. Li, Y. Yao, Z. Wang, J. Zhao, M. Zhao, C. Sun, Preparation of stable mesoporous silica FSM-16 from water glass in the presence of cetylpyridium bromide, Mater. Chem. Phys. 70 (2) (2001) 144–149.

[34] W. Lamouchi, S.B. Slama, F. Saadallah, M. Bouaicha, Nickel doping induced amorphization of brookite TiO_2: photoluminescence enhancement, Optik 227 (2021), 166123.

[35] J. Tientong, S. Garcia, C.R. Thurber, T.D. Golden, Synthesis of nickel and nickel hydroxide nanopowders by simplified chemical reduction, J. Nanotechnol. 2014 (2014).

[36] G.A. Gohar, T. Manzoor, A. Ahmad, H. Raza, A. Farooq, I. Karim, W. Iftikhar, M. Umar, F. Asad, Synthesis and investigate the properties of Cu–Al–Ni alloys with Ag addition using powder metallurgy technique, J. Alloys Compd. 817 (2020), 153281.

[37] H. Far, M. Hamici, N. Brihi, K. Haddadi, M. Boudissa, T. Chihi, M. Fatmi, High-performance photocatalytic degradation of NiO nanoparticles embedded on α-Fe_2O_3 nanoporous layers under visible light irradiation, J. Mater. Res. Technol. 19 (2022) 1944–1960.

[38] M.A. Mahdi, L.S. Jasim, M. Ranjeh, M. Masjedi-Arani, M. Salavati-Niasari, Improved pechini sol-gel fabrication of $Li_2B_4O_7$/NiO/$Ni_3(BO_3)_2$ nanocomposites to advanced photocatalytic performance, Arab. J. Chem. 15 (5) (2022), 103768.

[39] D. Tian, Z. Liu, D. Li, H. Shi, W. Pan, Y. Cheng, Bimetallic Ni–Fe total-methanation catalyst for the production of substitute natural gas under high pressure, Fuel 104 (2013) 224–229.

[40] I. Fatimah, L. Sopia, Preparation of TiO_2/MCM-41 photocatalyst using rice husk ash as silica source, in: AIP Conference Proceedings, AIP Publishing LLC, 2017, 020124.

[41] S. Sugiyama, Y. Kato, T. Wada, S. Ogawa, K. Nakagawa, K.-I. Sotowa, Ethanol conversion on MCM-41 and FSM-16, and on Ni-Doped MCM-41 and FSM-16 prepared without hydrothermal conditions, Top. Catal. 53 (7) (2010) 550–554, https://doi.org/10.1007/s11244-010-9485-9.

[42] B. Rahimi, N. Jafari, A. Abdolahnejad, H. Farrokhzadeh, A. Ebrahimi, Application of efficient photocatalytic process using a novel BiVO/TiO_2-NaY zeolite composite for removal of acid orange 10 dye in aqueous solutions: modeling by response surface methodology (RSM), J. Environ. Chem. Eng. 7 (4) (2019), 103253.

[43] S. Bose, B. Kumar Tripathy, A. Debnath, M. Kumar, Boosted sono-oxidative catalytic degradation of Brilliant green dye by magnetic $MgFe_2O_4$ catalyst: degradation mechanism, assessment of bio-toxicity and cost analysis, Ultrason. Sonochem. 75 (2021), 105592.

[44] P. Badhai, S. Kashyap, S.K. Behera, Adsorption of phenol red onto GO-Fe_3O_4 hybrids in aqueous media, Environ. Nanotechnol. Monit. Manag. 13 (2020), 100282.

[45] A. Mittal, D. Kaur, A. Malviya, J. Mittal, V.K. Gupta, Adsorption studies on the removal of coloring agent phenol red from wastewater using waste materials as adsorbents, J. Colloid Interface Sci. 337 (2) (2009) 345–354.

[46] A. Kumar, C.J. Raorane, A. Syed, A.H. Bahkali, A.M. Elgorban, V. Raj, S.C. Kim, Synthesis of TiO_2, TiO_2/PAni, TiO_2/PAni/GO nanocomposites and photodegradation of anionic dyes Rose Bengal and thymol blue in visible light, Environ. Res. 216 (2023), 114741.

[47] M.A.E. Wafi, M.A. Ahmed, H.S. Abdel-Samad, H.A.A. Medien, Exceptional removal of methylene blue and p-aminophenol dye over novel TiO_2/RGO nanocomposites by tandem adsorption-photocatalytic processes, Mater. Sci. Energy Technol. 5 (2022) 217–231.

[48] A.N. Chishti, Z. Ma, Y. Liu, M. Chen, J. Gautam, F. Guo, L. Ni, G. Diao, Synthesis of highly efficient and magnetically separable Fe_3O_4@C-TiO_2-Ag catalyst for the reduction of organic dyes and 4-nitrophenol, Colloid Surf. A Physicochem. Eng. Asp. 631 (2021), 127694.

[49] F. Torki, H. Faghihian, Sunlight-assisted decomposition of cephalexin by novel synthesized NiS-PPY-Fe_3O_4 nanophotocatalyst, J. Photochem. Photobiol. Chem. 338 (2017) 49–59.
[50] M.F. Majnis, O.C. Yee, M.A. Mohd Adnan, M.R. Yusof Hamid, K.Z. Ku Shaari, N. Muhd Julkapli, Photoactive of Chitosan-ZrO_2/TiO_2 thin film in catalytic degradation of malachite green dyes by solar light, Opt. Mater. 124 (2022), 111967.
[51] Y. Vasseghian, M. Moradi, M. Pirsaheb, A. Khataee, S. Rahimi, M.Y. Badi, A. Mousavi Khaneghah, Pesticide decontamination using UV/ferrous-activated persulfate with the aid neuro-fuzzy modeling: a case study of Malathion, Food Res. Int. 137 (2020), 109557.
[52] Z. Talebzadeh, M. Masjedi-Arani, O. Amiri, M. Salavati-Niasari, La2Sn2O7/g-C3N4 nanocomposites: rapid and green sonochemical fabrication and photo-degradation performance for removal of dye contaminations, Ultrason. Sonochem. 77 (2021), 105678.
[53] Z. Guo, R. Zhan, Y. Shi, D. Zhu, J. Pan, C. Yang, Y. Wang, J. Wang, Innovative and green utilization of zinc-bearing dust by hydrogen reduction: recovery of zinc and lead, and synergetic preparation of Fe/C micro-electrolysis materials, Chem. Eng. J. 456 (2023), 141157.
[54] W. Guo, H. Luo, Z. Jiang, D. Fang, J. Chi, W. Shangguan, Z. Wang, L. Wang, A.F. Lee, Ge-doped cobalt oxide for electrocatalytic and photocatalytic water splitting, ACS Catal. 12 (19) (2022) 12000–12013.
[55] R.R. Mathiarasu, A. Manikandan, K. Panneerselvam, M. George, K.K. Raja, M.A. Almessiere, Y. Slimani, A. Baykal, A.M. Asiri, T. Kamal, A. Khan, Photocatalytic degradation of reactive anionic dyes RB5, RR198 and RY145 via rare earth element (REE) lanthanum substituted $CaTiO_3$ perovskite catalysts, J. Mater. Res. Technol. 15 (2021) 5936–5947.
[56] B. Rahimi, N.R. Rahimi, A. Ebrahimi, Catalytic reduction of hazardous acid orange 10 dye by $BiVO_4$/TiO_2 nanocrystalline heterojunction and influence of aeration, $FeSO_4$, H_2O_2 and $FeCl_3$ on removal efficiency: a novel and environmentally friendly process, Arab. J. Chem. 15 (8) (2022), 104003.
[57] H. Eckert, M. Bobeth, S. Teixeira, K. Kühn, G. Cuniberti, Modeling of photocatalytic degradation of organic components in water by nanoparticle suspension, Chem. Eng. J. 261 (2015) 67–75.
[58] P.M. Martins, V. Gomez, A.C. Lopes, C.J. Tavares, G. Botelho, S. Irusta, S. Lanceros-Mendez, Improving photocatalytic performance and recyclability by development of Er-Doped and Er/Pr-codoped TiO_2/Poly(vinylidene difluoride)–Trifluoroethylene composite membranes, J. Phys. Chem. C 118 (48) (2014) 27944–27953, https://doi.org/10.1021/jp509294v.
[59] R. Beura, P. Thangadurai, Effect of Sn doping in ZnO on the photocatalytic activity of ZnO-Graphene nanocomposite with improved activity, J. Environ. Chem. Eng. 6 (4) (2018) 5087–5100.
[60] Z. Mengting, T.A. Kurniawan, S. Fei, T. Ouyang, M.H.D. Othman, M. Rezakazemi, S. Shirazian, Applicability of $BaTiO_3$/graphene oxide (GO) composite for enhanced photodegradation of methylene blue (MB) in synthetic wastewater under UV–vis irradiation, Environ. Pol. 255 (2019), 113182.
[61] N. Almulhem, C. Awada, N.M. Shaalan, Photocatalytic degradation of phenol red in water on Nb (x)/TiO_2 nanocomposites, Crystals 12 (7) (2022) 911.
[62] S. Belattar, N. Debbache, I. Ghoul, T. Sehili, A. Abdessemed, Photodegradation of phenol red in the presence of oxyhydroxide of Fe (III)(Goethite) under artificial and a natural light, Water Environ. J. 32 (3) (2018) 358–365.
[63] H.S. Wahab, A.A. Hussain, Photocatalytic oxidation of phenol red onto nanocrystalline TiO_2 particles, J. Nanostruct. Chem. 6 (2016) 261–274.